Rare Metal Materials and Engineering
Volume 50, Issue 11, November 2021
Available online at www.rmme.ac.cn

Science Press

Cite this article as: Xia Yelin, Huang Zhaozhen, Chen Hanning, et al. In-situ Spectral Monitoring of Microstructure During Laser Melting Deposition: A Case Study of CoCrMoW Alloy[J]. Rare Metal Materials and Engineering, 2021, 50(11): 3901-3909.

ARTICLE

In-situ Spectral Monitoring of Microstructure During Laser Melting Deposition: A Case Study of CoCrMoW Alloy

Xia Yelin[1], Huang Zhaozhen[1], Chen Hanning[1,2], Liang Xiaodan[2], Shi Chuan[3]

[1] School of Mechanical Engineering, Tiangong University, Tianjin 300387, China; [2] School of Computer Science and Technology, Tiangong University, Tianjin 300387, China; [3] Institute for Applied Materials, Karlsruhe Institute of Technology, Karlsruhe 12, 76131, Germany

Abstract: The relationship between the optical emission spectroscopy and the microstructure of CoCrMoW coatings by laser melting deposition was investigated. The relationship between the primary dendrite spacing and microhardness of CoCrMoW coatings at different laser powers of spectral signal was studied. A new spectral signal index, the integral area, was proposed, and the electron temperature was calculated from four discrete Cr I spectral lines. The results show that with increasing the laser power from 400 W to 1000 W, the average primary dendrite spacing is increased from 3.426 μm to 7.420 μm, and the microhardness $HV_{0.2}$ is reduced from 3461 MPa to 3095 MPa. The integral area and electron temperature of the spectral is also increased with increasing the laser power. The primary dendrite spacing of the coating is positively linear-related with the spectral signal, while the microhardness of the coatings is negatively linear-related with the spectral signal. In this research, compared with the electron temperature, the integral area shows a better potential for the prediction of the primary dendrite spacing and microhardness of coatings.

Key words: laser melting deposition; optical emission spectroscopy; CoCrMoW coating; integral area; electron temperature

CoCr alloy has been used in aero-engine, turbine blade[1,2], and bioimplants, such as denture and artificial joints[3,4], due to its high-temperature strength, high wear resistance, excellent corrosion resistance, and biocompatibility. Traditional manufacturing methods used in metal implants, including casting, cutting, and hot pressing, can lead to high defect, low material utilization, a long production cycle, and high cost[5,6]. In recent years, the laser-based additive manufacturing (AM) methods, such as selective laser melting (SLM) and laser melting deposition (LMD), have attracted wide attention, because they can overcome many shortcomings of traditional manufacturing methods and offer a way for feasible manufacturing of parts with complex structure. Thus, the laser-based AM has gradually become one of the most important methods for repairment and fabrication of objects with 3D structure[7].

It is known that the mechanical properties of CoCr alloys, such as tensile properties, wear resistance, and microhardness, are determined by their microstructure. For example, Qian et al[8] reported that the Vickers hardness and tensile strength of CoCrMo alloy fabricated by SLM are better than those made by casting. The improvement is caused by the heterogeneous multiscale (from macroscale to nanoscale) textures formed by SLM. Lee et al[9] found that the microstructures (crystal orientation) determine the anisotropic mechanical properties of SLMed CoCrW alloys. Hedberg et al[10] found that the SLMed CoCrMo specimens show better corrosion resistance than the cast ones do due to the rapid cooling and fine cellular structure. Ram et al[11] found that the wear resistance of laser cladded CoCrMo alloy is affected by the number and morphology of cemented carbide particles in the microstructure. In general, almost all these metallographic specimens need to be carefully prepared (machined and etched) to characterize the microstructure. Ideally, the manufactured specimen should be non-destructive and prepared without complex preparation procedures.

Recently, in order to improve the quality and reliability of parts manufactured by laser-based AM, much attention is paid

Received date: November 02, 2020
Foundation item: National Key R&D Program of China (2017YFB1103604); National Natural Science Foundation of China (61772365); Tianjin Province Science and Technology Projects (17JCQNJC04500, 17JCYBJC15100)
Corresponding author: Chen Hanning, Ph. D., Professor, School of Mechanical Engineering, Tiangong University, Tianjin 300387, P. R. China, E-mail: perfect_chn@hotmail.com

on real-time monitoring techniques[12,13]. For example, the optical emission spectroscopy is applied to real-time monitoring using the plasma produced by the interaction between the laser and metal powder. Song[14] and Shin[15] et al established the relationship between plasma parameters and elemental composition by analyzing element spectral lines, which achieved the real-time detection of elements the LMD process. Lednev et al[16,17] showed the in-situ quantitative analysis of key elements by laser-induced breakdown spectroscopy in LMD. Ya et al[18] studied the spectral signal of the onset and extent of metallic bonding in LMD, and suggested that the electron temperature shows a better correlation with the dilution. Lough et al[19] developed a set of equipment for in-situ spectral detection during SLM and found that the temperature of the vapor plume is correlated with the melting pool size. Chen et al[20,21] established the LMD spectral diagnosis system to investigate the relationship between processing parameters and plasma radiation intensity and the related influence on forming quality. In brief, the spectral detection is mainly used for determination of element composition and surface quality analysis in AM. However, it is more important to establish a relationship among processing, structure, and mechanical properties.

In this research, an in-situ spectral monitoring system was established for manufacturing CoCrMoW alloy using LMD. The spectra of the melting pool at different laser powers were analyzed. The relationship among the spectral signal of the melting pool, primary dendrite spacing, and microhardness at different processing parameters using the integral area of spectral curve and electron temperature was established.

1 Experiment

In this study, CoCrMoW powders with size ranging from 45 μm to 106 μm were used. Fig. 1 shows the morphology of CoCrMoW alloy powers observed by scanning electron microscope (SEM). The elements of CoCrMoW alloy included Co, Cr, Mo, W, and Si, as shown in Table 1. CoCrMoW alloy powders were deposited on the Q235 steel substrate with a dimension of 210 mm×60 mm×10 mm.

In this study, a beam of continuous wave (CW) fiber laser (wavelength of 1064 nm) was used for LMD. The powder was fed into the melting pool through a coaxial nozzle using a RC-PGF-D powder feeder (Raycham, China). In the multi-track cladding experiment, the laser power was increased from 400 W to 1000 W with a step size of 200 W at a scanning speed of 8 mm/s, and the spot diameter was 2 mm. An overlap ratio of 50% and a powder feeding rate of 25 g/min were selected.

Table 1 Chemical composition of CoCrMoW alloy power (wt%)

Cr	Mo	Si	W	Co
24.52	4.82	0.61	5.12	Bal.

The spectra produced during laser cladding were collected by a flame miniature spectrometer (Ocean Optics, Flame-S) with an entrance slit of 25 μm. The spectrometer used a linear silicon charge transfer device array (Sony ILX 511) with 2048 pixels and an integration time of 10 ms. The detector was fixed on the laser head with an angle of about 80°, i.e., about 10° from the substrate, as indicated in Fig.2. The detector was focused on the melting pool. The spectrum was converged by the focusing lens onto the optical fiber with a diameter of 600 μm, then guided into the spectrometer, and finally converted into the required digital signal. OceanView software was used to control the parameters of spectrum acquisition and subsequent data processing.

Metallographic specimens were prepared to study the relationship between the spectral signal and the microstructure of the coating. SEM (ZEISS Sigma 300) and X-ray diffraction (XRD, D/MAX-2500, Cu target, 40 kV, 140 mA) were used to analyze the microstructure and phases of the coating. Microhardness of the coating was measured by HV-1000 Vickers hardness tester at load of 0.2 kg for loading time of 10 s. The collected spectra were analyzed offline to identify the discrete spectra, and then the integral area and electron temperature signals were used for further study.

2 Results and Discussion

2.1 Microstructure of multi-track coating

Fig.3 shows SEM images of CoCrMoW coatings prepared

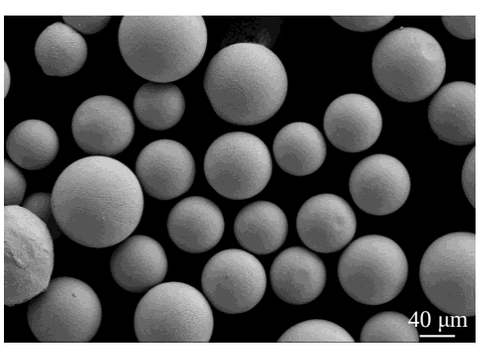

Fig.1 SEM morphology of CoCrMoW alloy powder

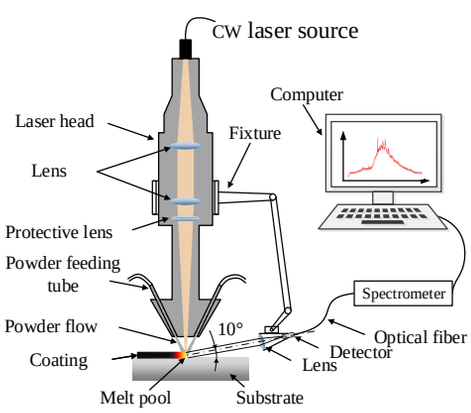

Fig.2 Schematic diagram of experiment device

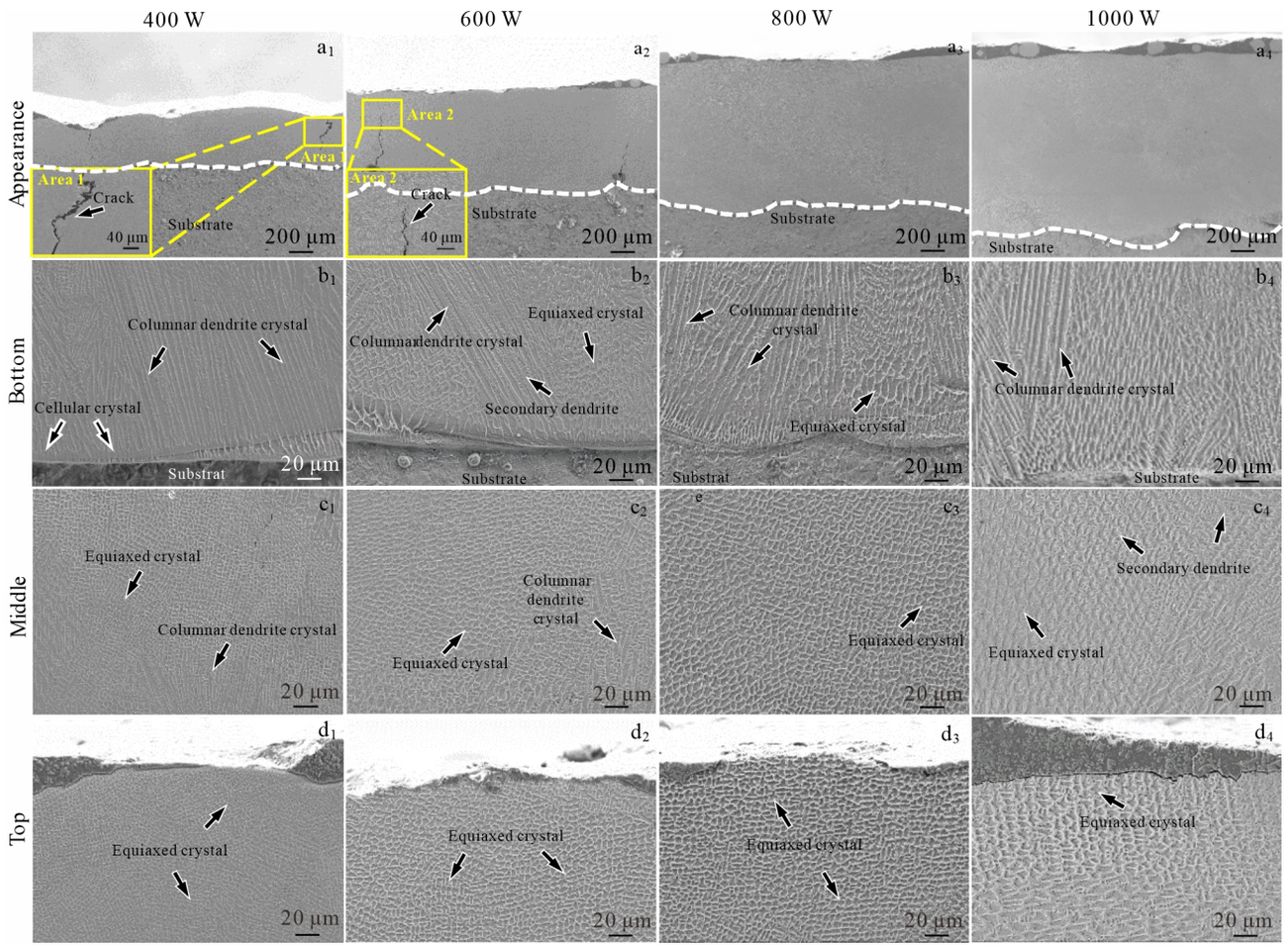

Fig.3 SEM images of appearances (a_1~a_4), bottom (b_1~b_4), middle (c_1~c_4), and top (d_1~d_4) parts of CoCrMoW coatings at different laser powers: (a_1, b_1, c_1, d_1) 400 W, (a_2, b_2, c_2, d_2) 600 W, (a_3, b_3, c_3, d_3) 800 W, and (a_4, b_4, c_4, d_4) 1000 W

at different laser powers with a constant scanning speed of 8 mm/s. It is obvious that the average coating thickness is increased from 0.37 mm to 1.23 mm with increasing the laser power from 400 W to 1000 W, as indicated in Fig. 3a_1~3a_4. Due to the rapid melting and solidification of powders in LMD, the microstructure can be determined by constitutional supercooling theory[22], indicating that the liquid temperature is lower than the liquidus temperature, which is related to temperature gradient G and solidification rate R. It can be expressed by Eq.(1) and Eq.(2), as follows[23]:

$$G = \frac{2K\left(T - T_0\right)^2}{\varepsilon P} \tag{1}$$

$$R = V_s \cos\theta \tag{2}$$

where K is the thermal conductivity of alloy, T is liquid temperature of alloy, T_0 is initial temperature of substrate, ε is absorption efficiency of laser, P is laser power, V_s is laser scanning speed, θ is the included angle between V_s and R. During LMD, the cooling rate GR determines the grain size of solidified structure with an inversely proportional relationship. It is also known that the morphology of the solidified structure is affected by G/R. With the decrease of G/R, the degree of constitutional supercooling is increased, and the solidification mode changes from planar to cellular and columnar crystal, and finally to equiaxed crystal[22]. The primary dendrite spacing δ reflects the extent of refinement of the microstructure, which is related to G and R. It can be expressed by Eq.(3), as follows[23]:

$$\delta = \frac{a}{\sqrt{GR}} \tag{3}$$

where a is a coefficient.

It can also be seen from Fig. 3a_1~3a_4 that the cracks appear at 400 and 600 W, but disappear at 800 and 1000 W. This may be due to the high-temperature gradient G; when the laser power is low, it results in the high residual stress of the coating and then the crack[24].

At the bottom part of coating, as shown in Fig. 3b_1~3b_4, the heat is mainly dissipated through the substrate. Columnar dendrite crystals grow from the bottom of the melting pool because of the large temperature gradient G and a small extent of constitutional supercooling in this area. The growth direction of columnar dendrite crystals is mostly along the temperature gradient direction which is perpendicular to the boundary of the melting pool[25].

The average primary dendrite spacing is determined by the number of grains passing through a straight line of a certain length, as shown in Fig.4. When the laser power is 400 W, the average primary dendrite spacing of columnar dendrite crystals in bottom part of coating is 4.538 μm, as listed in Table 2. With increasing the laser power to 600, 800, and 1000 W, the average primary dendrite spacing in bottom part of coating is 4.969, 5.856, and 7.020 μm, respectively. This change can be explained by the fact that the cooling rate *GR* is decreased with increasing the laser power, leading to a coarser microstructure. Meanwhile, the primary dendrite spacing is increased with decreasing the *GR*, according to Eq.(3).

Fig. $3c_1$~$3c_4$ show the microstructure of middle part of coatings. When the laser power is 400 and 600 W, the microstructures are mainly equiaxed crystals with a small number of columnar dendrite crystals. This is because the *G*/*R* value decreases rapidly from the bottom part to the middle part of the melting pool. Correspondingly, the columnar dendrite crystals are transformed into equiaxed crystals[26]. When the power is 800 and 1000 W, uniform equiaxed crystals are formed in the middle of the coating, and the grain size of equiaxed crystal continues to grow. For equiaxed crystals, the primary dendrite spacing can be regarded as their grain size, so it is observed that the average primary dendrite spacing is increased from 2.939 μm to 7.014 μm with increasing the laser power from 400 W to 1000 W, as shown in Table 2.

Fig. $3d_1$~$3d_4$ show the microstructures of the top part of coatings. It can be seen that almost all the microstructures in this region are equiaxed crystals at different laser powers. At the top part of coatings, the main heat dissipation mode is heat transfer inside the coating and heat convection on the surface. Therefore, the cooling rate and solidification rate in this region is fast and fine equiaxed grains are obtained. The average primary dendrite spacing of equiaxed crystals is increased significantly from 2.801 μm to 8.225 μm with increasing the laser power from 400 W to 1000 W, as shown in Table 2. In general, the average primary dendrite spacing is increased from 3.426 μm to 7.420 μm with increasing the laser power from 400 W to 1000 W.

2.2 Phase analysis

The phase component of CoCrMoW coatings at different powers is analyzed by XRD. The influence of laser power on phase component is presented in Fig. 5a. The XRD patterns show the presence of γ and ε phases with different grain orientations[27-30], and the change of laser power has little effect on the types of the main phases. Fig. 5b shows that the peak position of the phase shifts with the increase of laser power. When the power is 400, 600, 800, and 1000 W, the peak position is 43.62°, 43.84°, 43.56°, and 43.78°, respectively.

Table 2 Primary dendrite spacing of CoCrMoW coatings at different laser powers (μm)

Region	Laser power/W			
	400	600	800	1000
Bottom	4.538	4.969	5.856	7.020
Middle	2.939	5.176	5.355	7.014
Top	2.801	4.544	5.176	8.225
Average value	3.426	4.896	5.462	7.420

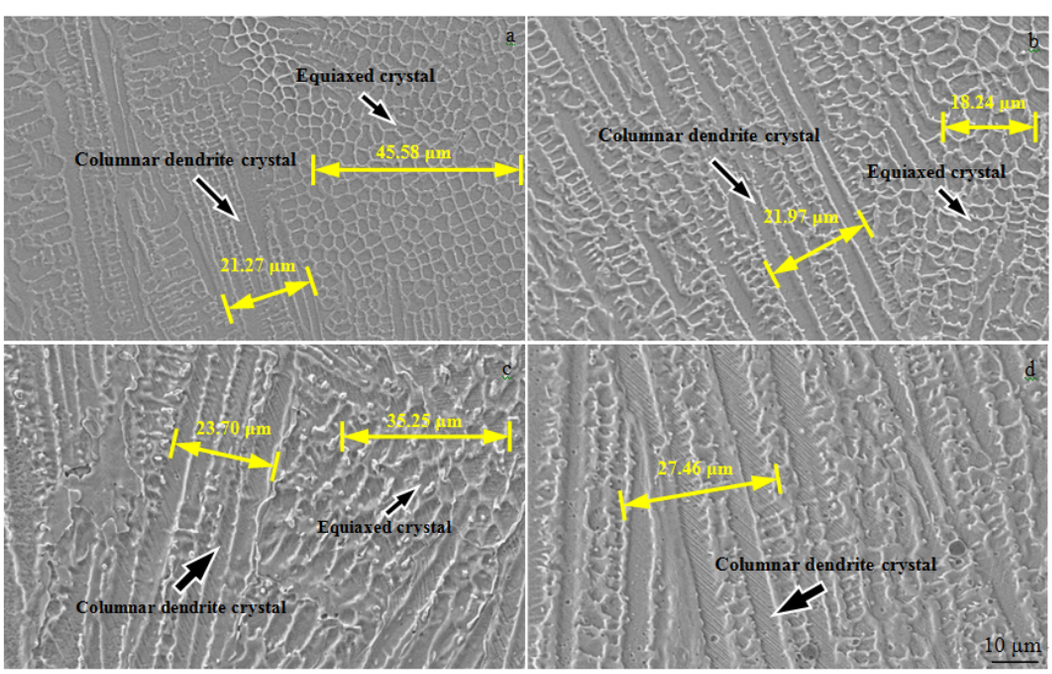

Fig.4 Primary dendrite spacing of CoCrMoW of coatings at different laser powers: (a) 400 W, (b) 600 W, (c) 800 W, and (d) 1000 W

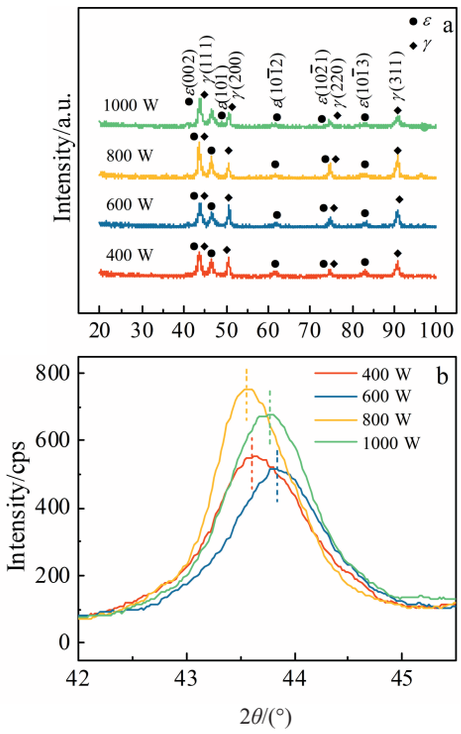

Fig.5 XRD patterns of different CoCrMoW coatings at 2θ=20°~100° (a) and 2θ=42°~44.5° (b)

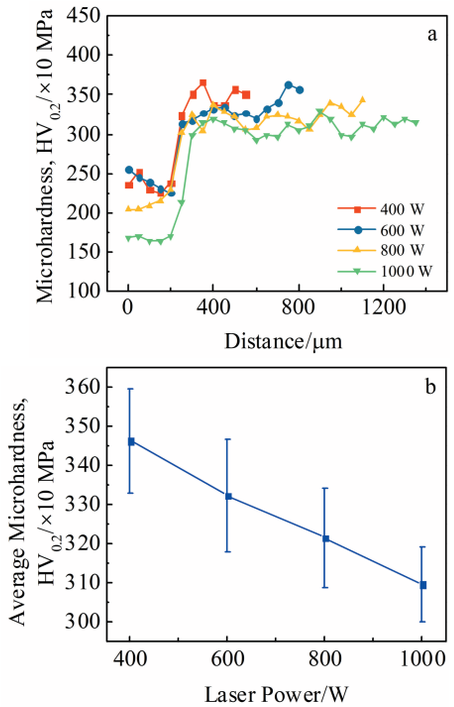

Fig.6 Microhardness $HV_{0.2}$ of different CoCrMoW coatings (a); relationship between average microhardness and laser power (b)

This may be due to the shrinkage of lattice anisotropy and lattice distortion caused by residual stress, which makes the diffraction peak shift to a small angle[31]. However, when the residual stress is released, the diffraction peak shifts to a large angle at laser power of 400 and 600 W. The diffraction angle is related to the inter-plane distance, according to Bragg's Law[32], as expressed by Eq.(4):

$$2d\sin\theta=n\lambda \quad (n=1,2,3\cdots) \tag{4}$$

where d is the inter-plane distance, θ is half scattering angle, and λ is the X-ray wavelength. The inter-plane distance shows negative correlation with the diffraction angle. Consequently, the inter-plane distance of CoCrMoW coatings decreases at first, then increases, and decreases finally.

Meanwhile, the full-width half-maximum (FWHM) of the diffraction peaks is decreased with increasing the laser power from 400 W to 1000W, as shown in Fig.5b. According to the Scherrer formula[33], as expressed by Eq.(5):

$$L=\frac{K\lambda}{\beta\cos\theta} \tag{5}$$

where L is the average grain size, K is a constant related to grain shape, and β is FWHM. Therefore, FWHM is inversely proportional to the average grain size, and the average grain size is decreased with increasing the laser power.

2.3 Microhardness

Fig.6a shows the microhardness of the coating at different positions, and a clearly increasing microhardness can be observed in the coating. The average microhardness $HV_{0.2}$ is reduced from 3461 MPa to 3095 MPa with increasing the laser power from 400 W to 1000 W. When the laser power increases from 400 W to 1000 W, the grain size increases as the solidification rate decreases, as shown in Fig.3. According to the Hall-Petch relationship[34], it is expected that the microhardness gradually decreases, as shown in Fig. 6b. Interestingly, the microhardness decreases almost linearly with a constant decrement of about 4% after increasing the laser power by 200 W each time. The result of a linear relationship can be a good sign for accurate prediction.

2.4 Spectra of melting pool

2.4.1 Integral area of spectral curve

The original spectra of CoCrMoW alloys obtained during LMD at different laser powers are shown in Fig.7a. Under the laser cladding condition, the major component of the optical emission is Planck's radiation of the melt pool surface, and thus a possible reason for the continuous background is the thermal radiation from the surface. The spectral lines are produced by the transition of electrons from high energy level m to low energy level n[35]. The spectral intensity I_{mn} can be described as follows[18]:

$$I_{mn}=N_m A_{mn} h\upsilon_{mn} \tag{6}$$

where N_m is the population of the upper state m (cm^{-3}), A_{mn} is the transition probability, h is Planck's constant, and υ_{mn} is the frequency of a photon. Assuming that the plasma is at local thermal equilibrium, then the population of the upper state can be expressed by Boltzmann law[18], as expressed by Eq.(7):

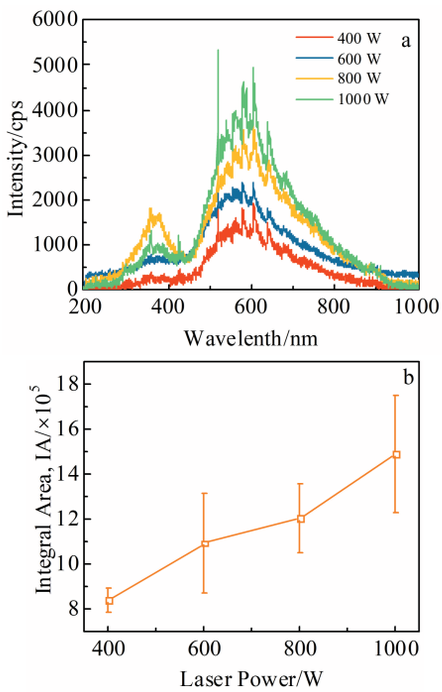

Fig.7 Original spectra (a) and integral area IA of spectra (b) at different laser powers

$$\frac{N_m}{N}=\frac{g_m}{Z(T_e)}\exp\left(-\frac{E_m}{kT_e}\right) \quad (7)$$

where N is the population of ground state particles (cm^{-3}), T_e is the electron temperature of the plasma (K), $Z(T_e)$ is the partition function at T_e, g_m is the degeneracy of upper state m, E_m is the energy of upper state m (cm^{-1}), and k is the Boltzmann constant.

It is known that in thermal radiation field, Planck's formula describes the relationship between the emissivity and frequency of electromagnetic radiation emitted from a blackbody. Stefan Boltzmann's law states the total energy radiated by a blackbody surface per unit area across all wavelengths per unit time, which can be obtained by integrating Planck's formula over the entire spectrum[36].

The spectral intensity I_{mn} in the whole monitored wavelength range is integrated without background subtraction, while the continuous background radiation is treated as noise which needs to be deducted in normal spectral analysis. The total integral area IA of the spectra can be obtained, as shown in Fig. 7b, which is regarded as the total radiation intensity in this range. With increasing the laser power from 400 W to 1000 W, IA is increased almost linearly from 8.392×10^5 to 14.879×10^5. It can be seen that the spectral continuum is the main factor for the increase of the integral area, which is closely related to the temperature of plasma.

2.4.2 Electron temperature

Electron temperature is an important parameter to characterize plasma produced by the interaction between laser and metal powder, which reflects the thermal input of laser. Electron temperature can be calculated by the relative intensities of discrete spectral lines by the Boltzmann plot method[18]. In the calculation, the continuous spectrum should be eliminated to reduce the error. Thus, the iterative stripping method[37] was used for background treatment.

By comparing the intensity I_i of a wavelength i and the average value of two adjacent sampling points in the spectrum, the rapid changing information in the spectrum can be stripped[37]. The flow chart of the background subtraction algorithm using iterative stripping is shown in Fig. 8. Then, by substituting Eq. (7) into Eq. (6), after some mathematical treatments, Eq.(6) can be expressed as follows:

$$\ln\left(\frac{I_{mn}\lambda_{mn}}{g_m A_{mn}}\right)\propto \ln\frac{Nhc}{Z(T_e)}-\frac{1}{kT_e}E_m \quad (8)$$

where λ_{mn} is the wavelength of the spectral line (nm), c is the light speed (m/s). Eq. (8) shows a linear relationship between $\ln(I_{mn}\lambda_{mn}/g_m A_{mn})$ and E_m, where $\ln(Nhc/Z(T_e))$ is a constant.

Thus, the electron temperature T_e can be estimated from the inverse of the slope $-1/(kT_e)$ fitted from the calculated data of multiple spectral lines, as shown in Fig. 9a. The parameters used for calculation in Eq. (8) can be found in National Institute of Standards and Technology (NIST) database. To ensure the calculation accuracy, the energy level difference between the two spectral lines used for calculation should be

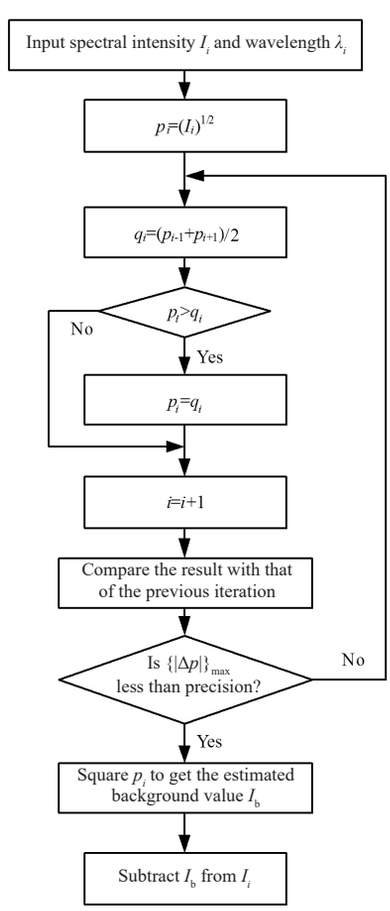

Fig.8 Algorithm flow chart of iterative stripping

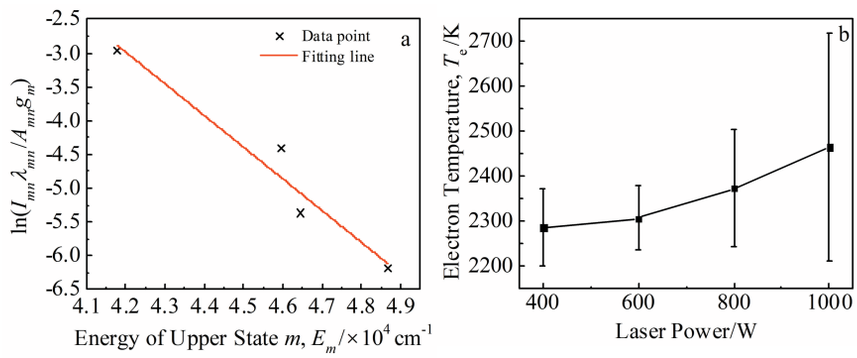

Fig.9 Boltzmann plot using four Cr I lines at 400 W (a); electron temperature at different laser powers (b)

as large as possible. Table 3 shows the spectral data of four selected Cr I lines at 400 W because some parameters of other lines required in Eq. (8) are not specified in NIST database. The calculated electron temperatures in Fig. 9b are increased almost linearly from 2286.206 K to 2463.742 K with increasing the laser power from 400 W to 1000 W.

2.4.3 Spectral intensity

Fig. 10 shows the intensity of spectral lines at different laser powers. Three spectral lines with the wavelength of 520.017, 580.022, and 605.513 nm were selected because of their appropriate intensities, FWHM, as well as less interference. It can be clearly seen that the intensities of three chosen spectral lines are increased with increasing the laser power. The reason for this phenomenon can be explained by Eq. (6) and Eq. (7). Once the spectral line is determined, its intensity is mainly related to the population of ground state particles N and the electron temperature T_e. When the laser power increases and other processing parameters remain unchanged, there is no clear change of the population of ground state particles N. Thus, the increasing electron temperature, as shown in Fig. 9b, is the main factor in increasing the spectral line intensity[20].

2.5 Relationship between spectrum signal and microstructure

The relationship between the spectral related information (integral area IA and average electron temperature T_e) and microstructures (average primary dendrite spacing δ and average microhardness) of the CoCrMoW coatings are shown in Fig. 11. It can be clearly seen that all the four fitting curves have linear relationships. Moreover, the integral area and electron temperature are positively correlated with the primary dendrite spacing δ of CoCrMoW coatings, as shown in Fig. 11a and 11c; while they are negatively correlated with the microhardness of CoCrMoW coatings, as shown in Fig. 11b and 11d. This is because the microstructure and integral area are closely related to the melting pool. The microstructure is formed after the melting pool solidifies, and the spectral signal radiated from the melting pool is determined by the state of the melting pool which is related to the heat input of laser. The increase of heat input leads to the increase of electron temperature, which promotes the collisional excitation of particles, increases the number of excited state particles, radiates more photons through energy level transition, and finally leads to the increase of the spectral intensity radiated from the melting pool. Thus, the larger integral area IA and higher electron temperature T_e can directly reflect the increasing heat input, which leads to the grain coarsening and reduces the microhardness of the coatings. The results show that the linearity of relationship corresponding to the integral area is more obvious than that corresponding to electronic temperature due to the larger R-Square, namely higher accuracy.

Table 3 NIST data of four selected Cr I lines at 400 W

λ_{mn}/nm	A_{mn}/s^{-1}	g_m	E_m/cm^{-1}
534.044 69	1.45×10^7	3	46 448.629
544.240 69	3.90×10^6	5	45 966.360
569.474 04	1.40×10^7	7	48 661.508
571.981 57	4.96×10^5	9	41 782.131

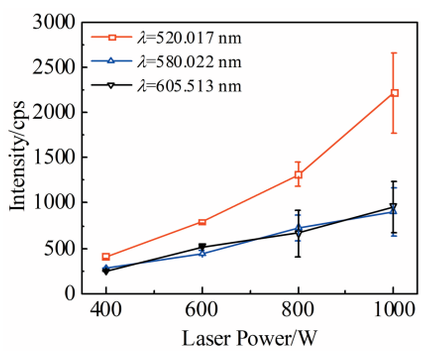

Fig.10 Spectral intensity of different wavelength at different powers

Therefore, the spectral signals can be used to predict the average primary dendrite spacing δ and average microhardness of CoCrMoW coatings processed by LMD. In addition, the integral area can directly reflect the heat input determined by the laser power without complex calculations. Thus, it can also be used to monitor LMD after calibration, and to avoid the inaccurate output power caused by the damage of optical lens or laser attenuation.

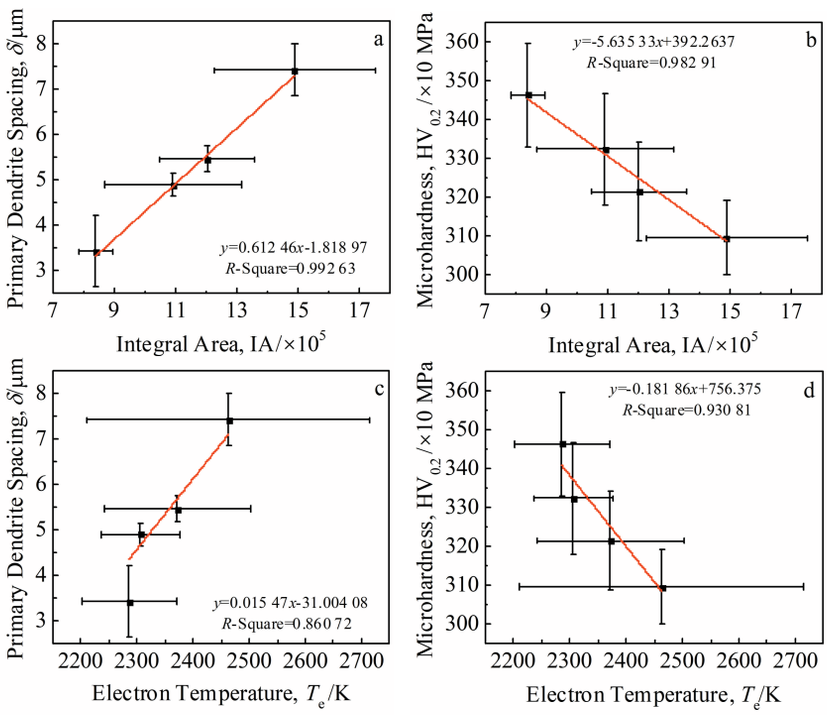

Fig.11 Relationship of average primary dendrite spacing δ-integral area IA (a), average microhardness-integral area IA (b), average primary dendrite spacing δ-electron temperature T_e (c), and average microhardness-electron temperature T_e (d)

3 Conclusions

1) The integral area of spectral curve proposed in this study and the electron temperature are increased almost linearly with increasing the laser power. However, the microhardness of CoCrMoW coating is decreased with increasing the laser power due to the coarsening of microstructure.

2) The spectral analyses indicate that the integral area show good capability for predicting the average primary dendrite spacing and the average microhardness of CoCrMoW coating. The results suggest that the spectral signal can be used to predict the microstructure (primary dendrite spacing and microhardness) of the coating.

References

1 Sun S H, Koizumi Y, Kurosu S *et al*. *Acta Mater*[J], 2014, 64: 154

2 Barekat M, Shoja Razavi R, Ghasemi A. *J Laser Appl*[J], 2016, 28(4): 42 005

3 Santecchia E, Gatto A, Bassoli E *et al*. *J Alloy Compd*[J], 2019, 797: 652

4 Lu Y J, Guo S, Yang Y *et al*. *J Alloy Compd*[J], 2018, 730: 552

5 Zhang M K, Yang Y Q, Song C H *et al*. *J Alloy Compd*[J], 2018, 750: 878

6 Liverani E, Fortunato A, Leardini A *et al*. *Mater Des*[J], 2016, 106: 60

7 Ahmadi S M, Hedayati R, Li Y *et al*. *Acta Biomater*[J], 2018, 65: 292

8 Qian B, Saeidi K, Kvetková L *et al*. *Dent Mater*[J], 2015, 31(12): 1435

9 Lee H W, Jung K H, Hwang S K *et al*. *Mater Sci Eng A*[J], 2019, 749: 65

10 Hedberg Y S, Qian B, Shen Z J *et al*. *Dent Mater*[J], 2014, 30(5): 525

11 Ram G D J, Esplin C K, Stucker B E. *J Mater Sci Mater Med*[J], 2008, 19(5): 2105

12 Song L J, Huang W K, Han X *et al*. *IEEE Trans Ind Electron*[J], 2016, 64(1): 633

13 Stutzman C B, Nassar A R, Reutzel E W. *Addit Manuf*[J], 2018, 21: 333

14 Song L, Mazumder J. *IEEE Sens J*[J], 2011, 12(5): 958

15 Shin J, Mazumder J. *Opt Laser Technol*[J], 2018, 106: 40

16 Lednev V N, Sdvizhenskii P A, Asyutin R D *et al*. *Opt Express* [J], 2019, 27(4): 4612

17 Lednev V N, Sdvizhenskii P A, Asyutin R D *et al*. *Addit Manuf* [J], 2019, 25: 64

18 Ya W, Konuk A R, Aarts R *et al*. *J Mater Process Technol*[J], 2015, 220: 276

19 Lough C S, Escano L I, Qu M *et al*. *Solid Freeform Fabrication* [C]. Austin: University of Texas, 2018: 2192

20 Chen B, Yao Y Z, Tan C W *et al*. *Int J Adv Manuf Technol*[J], 2018, 96(9-12): 4231

21 Chen B, Yao Y Z, Tan C W *et al*. *Transactions on Intelligent Welding Manufacturing*[M]. Singapore: Springer Singapore, 2018: 60

22 Kou S. *Welding Metallurgy*[M]. New York: Wiley, 2002
23 Huang Y J, Zeng X Y, Hu Q W *et al*. *Appl Surf Sci*[J], 2009, 255(7): 3940
24 Stutzman C B, Nassar A R, Reutzel E W. *Addit Manuf*[J], 2018, 21: 333
25 Wei H L, Elmer J W, DebRoy T. *Acta Mater*[J], 2017, 133: 10
26 Hemmati I, Ocelík V, De Hosson J T M. *J Mater Sci*[J], 2011, 46(10): 3405
27 Limmahakhun S, Oloyede A, Sitthiseripratip K *et al*. *Mater Des* [J], 2017, 114: 633
28 Barekat M, Razavi R S, Ghasemi A. *J Mater Eng Perform*[J], 2017, 26(7): 3226
29 Takaichi A, Nakamoto T, Joko N *et al*. *J Mech Behav Biomed Mater*[J], 2013, 21: 67
30 Béreš M, Silva C C, Sarvezuk P W C *et al*. *Mater Sci Eng A*[J], 2018, 714: 36
31 Ferreira N G, Abramof E, Corat E J *et al*. *Carbon*[J], 2003, 41(6): 1301
32 Wang Z Q, Denlinger E, Michaleris P *et al*. *Mater Des*[J], 2017, 113: 169
33 Vladescu A, Dinu M, Braic M *et al*. *Ceram Int*[J], 2015, 41(6): 8051
34 Wei X F, Li W J, Liang B J *et al*. *Tribol Int*[J], 2016, 97: 212
35 Ancona A, Spagnolo V, Lugarà P M *et al*. *Appl Opt*[J], 2001, 40(33): 6019
36 Kawai J, Ishii H. *Spectrochim Acta Part B: At Spectrosc*[J], 2005, 60(12): 1586
37 Wang Jingge, Li Xinzhong, Li Hehe *et al*. *Spectrosc Spectr Anal* [J], 2018, 38(1): 276 (in Chinese)

激光熔化沉积微观组织原位光谱监测:以CoCrMoW合金为例

夏椰林[1]，黄昭祯[1]，陈瀚宁[1,2]，梁晓丹[2]，石　川[3]
(1. 天津工业大学 机械工程学院，天津 300387)
(2. 天津工业大学 计算机科学与技术学院，天津 300387)
(3. 卡尔斯鲁厄理工学院 应用材料研究所，德国 卡尔斯鲁厄 12, 76131)

摘　要：研究了激光熔化沉积CoCrMoW涂层的微观组织与发射光谱的关系，及不同激光功率的光谱信号与CoCrMoW涂层一次枝晶间距、显微硬度的关系。提出了一种新的光谱信号指数积分面积，由4条离散Cr I谱线计算出电子温度。结果表明，当激光功率从400 W增加到1000 W，平均一次枝晶间距由3.426 μm增加到7.420 μm，显微硬度$HV_{0.2}$由3461 MPa降低到3095 MPa。光谱的积分面积和电子温度随激光功率的增大而增大。涂层的一次枝晶间距与光谱信号呈正相关，而涂层的显微硬度与光谱信号呈负线性相关。与电子温度相比，积分面积在预测一次枝晶间距和显微硬度方面显示出更好的潜力。

关键词：激光熔化沉积；发射光谱；CoCrMoW涂层；积分面积；电子温度

作者简介：夏椰林，男，1991年生，博士生，天津工业大学机械工程学院，天津 300387，E-mail：xiayelin2020@163.com